Direct measurement and modeling of spontaneous charge transfer across anatase–brookite nanoheterojunctions

Leonardo Lo Presti[1], Valentina Pifferi[1], Giovanni Di Liberto[1,2], Giuseppe Cappelletti[1], Luigi Falciola[1], Giuseppina Cerrato[3], and Michele Ceotto[1,*]

[1.] Department of Chemistry, Università degli Studi di Milano, via Golgi 19, 20133 Milano

[2.] Present address: Department of Materials Science, Università degli Studi di Milano–Bicocca, via Cozzi 55, 20125 Milano

[3.] Department of Chemistry, Università degli Studi di Torino, via Giuria 7, 10125 Torino

* To whom correspondence should be addressed: michele.ceotto@unimi.it

ABSTRACT: Nanocomposites are at the heart of the present nanotechnology revolution in several strategic fields, including Green Chemistry, sensors and pollutant remediation. The promising and extensively examined nanotitania photocatalysts have performances hampered by the rapid recombination of photogenerated charge carriers. By generalizing the 2D–heterojunctions physics to 3D patchworks of intimately associated anatase and brookite mixed crystallites (multi–phase polymorph, MPP), we explain a possible strategy to overcome this major limitation. The anatase/brookite composite material is fully characterized experimentally and by simulations. We demonstrate that the anatase–brookite interphase behaves as a ground–state nano-diode containing an almost ideal nanocapacitor, associated to a net transfer of electrons from anatase to brookite. Implications of the direct observation of a polarized interphase on the understanding of nanotitania photocatalysts at the atomic scale are discussed.

Introduction

The spontaneous recombination of photogenerated charge carriers is the main drawback that impacts negatively on the performances of photocatalytic materials,[1–4] especially in promising titania-based nanocrystals.[5,6] In this respect, extrinsic bulk impurity/defect states play a fundamental role,[5,7,8] as they can create shallow mid-gap states and reduce the apparent bandgap[9] at the expense of increasing the concentration of trapping centres[10] for electrons (e^-) and holes (h^+), which slow down the recombination rate.[11] Crystals of TiO_2 anatase can be also doped on their growing surfaces, to stabilize the metastable {001} facets over the thermodynamically favored, but less reactive, {101} ones.[12–14] However, neither doping or co-doping has turned pristine titania materials into efficient visible light catalyzers.[15,16] These approaches alone have not proven particularly

useful, which has led to the proposal of third generation materials consisting of either two or three interconnected semiconductor materials.[17–19]

An alternative strategy to fight the curse of recombination relies on hybrid materials, where different semiconductors are joined through a 2D–heterojunction, which spontaneously promotes a net flow of charge across the interface.[20,21] This is due to the thermodynamic drive toward the equilibration of the chemical potential of the two phases, under the continuity constraints imposed by the Poisson's equation.[22] The resulting quantum mechanical picture is that one of a 2D quantum well that traps some charge carriers at the junction, and produces an equilibrium electric double layer.[23] Any further transfer of electrons or holes across the phase boundaries is thus kinetically and thermodynamically hindered. A variety of layered photonic devices relying on this physics is well known, including light emitting diodes,[24] laser diodes,[25] photocatalysts,[21] and electro–analytical sensors.[26]

The charge vectorial displacement originated from the contact between phases is correlated to the e^-–h^+ recombination delay. In principle, even an interface between polymorphs of the same chemical system, like anatase and brookite phases of TiO_2, can act as a diode, as the valence and conduction band edges of the two bulk crystals are different[27]. However, the difference is often too small to be of any practical utility in macroscopic layered devices, which in fact are mostly composed by chemically different compounds[28].

We hypothesize that nano double–layers in multiphase nanostructured powders of TiO_2 might be exploited to boost the photocatalytic performances even in the absence of a composite (multi–layered) architecture. It has been substantiated again and again that heterogeneous mixtures of TiO_2 polymorphs with a predominance of anatase generally show greater photocatalytic yields than one–phase TiO_2 (See Section S7 SI).[29–32] Specifically, the photocatalytic visible-light performances of N-doped anatase are significantly enhanced in the presence of the brookite phase, even respect to

the rutile one[33–35]. This has been explained by invoking a lower recombination rate of charge carriers, which in turn has been attributed to band alignment effects, and a charge transfer across the phase boundaries.[36–38] However, this could be just a part of the story. Our idea is to take advantage of the intimate connection among nanocrystallites of anatase and brookite in well–defined ratios, whose nano-diode-like heterojunctions might cooperatively produce a net measurable equilibrium (ground–state) effect. In other words, we look for "multi–phase polymorphs" (MPP) nano–diodes. The latter are expected to spontaneously self–assemble between surfaces with similar meshes, such as the most stable $(101)_{anatase}$ and $(210)_{brookite}$ facets, which have almost commensurate translation periods (see below and Section S3.3 SI). To this end, we synthesized, characterized and tested multiple nanoheterojunctions in bulk N-doped anatase-brookite TiO_2 nanostructured powders (details of the experimental procedures are reported in Methods – see below – and in Section S1 of the Supplementary Information; SI). These materials afford an ideal test case to probe the role of the phase composition, as nanopowders with nm–size crystallites bear a very small concentration of bulk grain boundaries that may act as recombination centres,[39] and surface band bending is negligible.[40] The main roles of the non–metal N dopant are (i) to provide the visible light chromophore center and (ii) to control the amount of brookite: the higher the nominal N/Ti molar ratio, the higher the anatase content.[9,41] We show both experimental and computational evidences that statistically dispersed MPP nano–heterojunctions can cooperatively produce an effective capacitor layer, which is able to significantly improve the photocatalytic performances of the material under UV illumination. The paper is organized as follows. First, the equilibrium properties of the ground–state system are described based on the outcomes of high–grade DFT simulations and Electrochemical Impedance Spectroscopy measurements in the dark. Then, the response of the system is probed by photocurrent experiments under UV illumination and a principal component

4

analysis is performed to find relevant correlations among structural and composition parameters and recombination times. A final section summarizes the main findings and conclusions.

Results and Discussion

Explicit DFT modelling of the anatase:brookite main interface

Semiconductors with very similar band gaps and type (anatase: ~3.1 eV; brookite: ~3.3 eV) were chosen to create extremely intimate surface contacts of complex 3D networks of statistically oriented nanocrystallites (Figure 1a), in contrast to the artificial ones where the contact is created *ad hoc* on cm^2–scale surfaces. HR-TEM analyses (Figure 1a and Section S2 SI) demonstrate that the contact between the two phases occurs frequently through the association of the most stable[14,42] {101}$_{Anatase}$ and {210}$_{Brookite}$ facets. In particular, the electron diffraction of the overlapping portion of the two phases reveals the existence of {101}$_{Anatase}$:{210}$_{Brookite}$ nano–junctions among the nanocrystals. The electron diffraction pattern of the interphase region (Figure 1b) is the superimposition of the diffraction images ascribable to either (101) anatase and/or (210) brookite exposed planes. The corresponding meshes are very similar but differently oriented[43]. As shown in the SI (Sections S3.3 and S3.4), the 1x1 (210) brookite mesh is almost commensurate with a reconstructed 2x1 (101) anatase one, provided that the surfaces are mutually rotated by ~ 10 deg around the non–crystallographic direction. This implies that the reconstructed (101) anatase surface could serve as a template for the epitaxial growth of (210) brookite (Figure 2b); the energy gain due to brookite crystallization[44] is more than enough to pay the cost of the reconstruction at the interface. The large amount of (101):(210) contacts found by the HR–TEM analysis (see also Figure S1 SI), as well as the measured macroscopic capacitance (see below), suggest that such an intimate connection is more frequent than expected on a pure statistical basis. This can be explained by the

5

relative abundance of the most stable $\{101\}_{Anatase}$ and $\{210\}_{Brookite}$ surfaces, possibly coupled

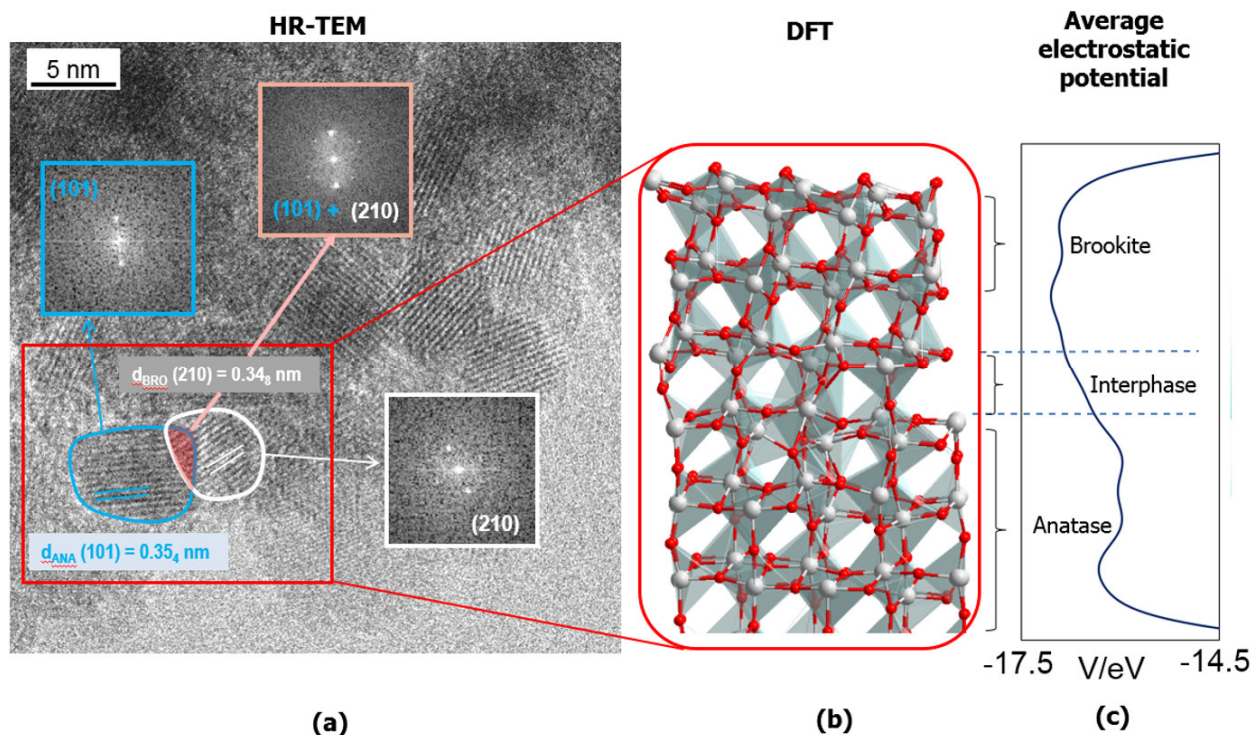through an epitaxy–driven heterogeneous nucleation mechanism.

Figure 1. From nanoparticle imaging to first-principles atomistic calculations. (a) HR–TEM image of anatase:brookite 77:23 *w/w* nanopowders (Section S2 SI). The insets represent the electron diffraction patterns relative to the two nanoparticles evidenced in blue (anatase) and white (brookite), respectively. The third electron diffraction, indicated as "Interface", refers to the overlapping region (evidenced in red) between the two above examined nanoparticles. The material is highly crystalline, with neatly visible interference fringes with periodicity of anatase (101) and brookite (210) crystallographic planes. Spheroidal crystallites have average estimated diameters of 4–8 nm and the two phases statistically dispersed in a homogeneous mixture. (b) Atomistic model of the structure of the $\{101\}_{anatase}$:$\{210\}_{brookite}$ interphase, fully relaxed at the DFT+U/PBE level of theory (see Methods and Section S3 SI). (c) Plane-averaged electrostatic potential (eV) for the mixed anatase/brookite system, as a function of the non–crystallographic Z coordinate, i.e. along the slab perpendicular.

Accordingly, we simulated the (101):(210) contact at the DFT/PBE+U level of theory (full details

in Section S3 SI). The optimized atomic arrangement presents a ~1 nm thick interphase layer

(Figure 1b), which is somewhat more reminiscent of the brookite bulk structure. This is confirmed

by the rumpling curve reported in Section S3.4 (Figure 6 SI), where the averaged root-mean-square

deviation (RMSD) of each atom position from the respective bulk one is reported. The anatase-like region recovers the original bulk arrangement after 1 nm from the contact region, while the brookite-like one after 0.4 nm. The slab dimensions are chosen large enough to describe all relevant rearrangements that are taking place at the interphase. The slab surface layer atoms in contact with the vacuum are kept frozen at the bulk geometry and they are under-coordinated. Thus, the interphase region is immune from the surface-vacuum interactions and the optimization is driven only by the anatase and brookite original bulk configurations. The polarization effects induced by this choice on both sides of the slab compensate each other. Thus, they do not influence the charge distribution of the interphase layer, as it can be appreciated from the plane–averaged electrostatic potential along the non–crystallographic direction (Figure 1c and Section S3.7 SI).

Electrochemical Impedance Spectroscopy measurements

Integration of the DFT ground–state charge density within the topological atomic basins defined according to the Quantum Theory of Atoms in Molecules[45] estimates a net transfer of ~ 0.5 electrons from the anatase to the brookite side of the interface (Figure 1c and S3.6 SI). Atomic charges are reported in Tables 1 and 2 of SI, and in Fig.S10a using a color code. These are relatively constant throughout the slab; no specific oxidizing or reducing centers can be found. Accordingly, we do not focus on individual atomic charges, whose calculation and interpretation are still an open issue.[46] Rather, the overall charge transfer between the two phases, which involves an electronic rearrangement in the whole anatase and brookite structures, is much more informative, as it can be also accessed experimentally by Electrochemical Impedance Spectroscopy (EIS, Figure 2). The systems were studied without the addition of any electrochemical probe, to evaluate only phenomena deriving from the electrode material, the support and the inert solution. Moreover, all the measurements were carried out in the absence of UV excitation, to probe just the ground–state

macroscopic properties of the MPP nanopowder. The potential was set to 0 V (SCE), very close to the open circuit potential of the electrochemical cell, to avoid phenomena driven by potential changes. The behaviour of FTO is very similar to that of a pure capacitor (vertical line with a slope very close to 90°, confirmed also by the corresponding Bode plot in Figure 2b). Instead, the oxide samples deviate from the linear trend, as expected. In Figure 2b more evidences for an additional RC element in the Anatase/Brookite sample are reported. While anatase sample presents two peaks, ascribable to RC of the two interphases, one with the solution and the other with support, the mixed anatase:brookite sample is very similar to the pure anatase one (given the predominant presence of anatase), but a third peak is appreciable between 1 and 10 Hz, related to a new anatase and brookite contact (the third interphase).
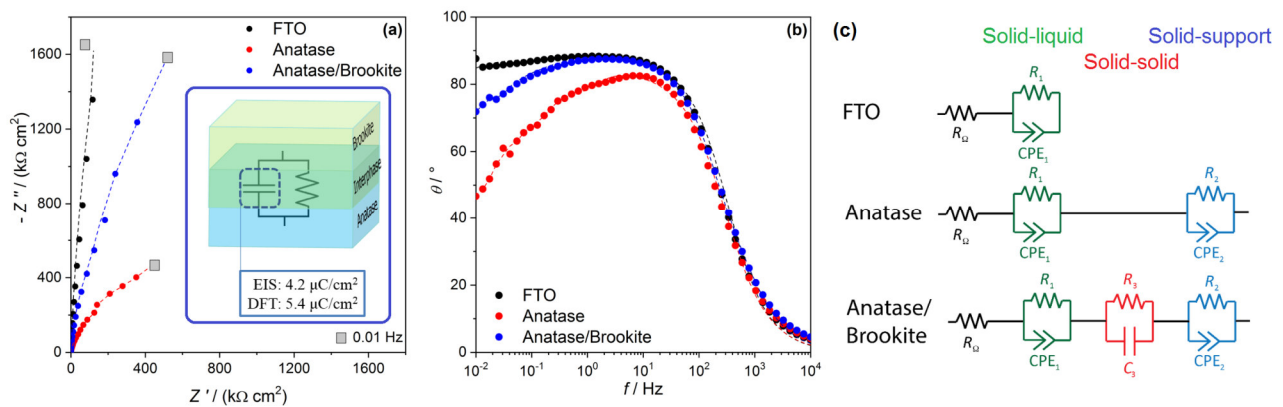

Figure 2. Complex–plane plots in panel (a) and phase Bode plots in panel (b) for the following samples: pristine support (Fluorine–doped Tin Oxide, FTO, black dots), pure anatase (Alfa Aesar 284, fifth row in Table 1, red dots), and anatase/brookite mixed oxide (T400, seventh row in Table 1, blue dots). Dashed lines represent the fitting, performed with the equivalent circuits showed in panel (c) for the solid–liquid (green), solid–solid (red) and solid–support (light blue) interfaces. Fitted parameters are shown in Table 1. Inset of panel (a): The double layer behaves as a nano–heterojunction where a complex 3D network of solid–solid interphases is acting as intimately associated nanoscale capacitors with EIS–estimated specific charge transfer of 4.2 μC·cm^{-2} (see Methods and Section S4 SI). The agreement with the DFT estimate of 5.4 μC·cm^{-2} is remarkable.

The experimental data were fitted (Figure 2b) using the equivalent circuits of one (FTO, support), two (pure anatase sample) and three (anatase/brookite sample) RC series (Figure 2c). The results

are summarized in Table 1. The capacitances at the interphases with the solution (CPE$_1$) and with the support (CPE$_2$) are fitted by a constant phase element CPE= $[(Ci\omega)^\alpha]^{-1}$, considering the inhomogeneous surface of the oxide layers and the consequent non–ideal capacitor contact.

Table 1. Fitted parameters for the circuit elements modelled as in Figure 2c. *C*: capacity; *R*: resistance; CPE: constant phase capacity element; α: exponent in CPE= $[(Ci\omega)^\alpha]^{-1}$ (see text).

Sample	R_Ω / (Ω cm²)	CPE$_1$ / (µF cm⁻² s$^{\alpha-1}$)	α_1	R_1 / (kΩ cm²)	C_3 / (µF cm⁻²)	R_3 / (Ω cm²)	CPE$_2$ / (µF cm⁻² s$^{\alpha-1}$)	α_2	R_2 / (MΩ cm²)
	Liquid	Solid–liquid interface			Solid–solid interface		Solid–support interface		
FTO	70.8	8.2	0.98	35.0	–	–	–	–	–
Anatase	86.6	65.6	0.99	1.1	–	–	10.9	0.93	0.4
Ana/Bro	67.7	47.8	0.89	42.9	19.6	13.1	9.9	0.99	2.6

R$_1$ shows a typical value of oxide/solution interphase, while R$_2$ is greater, as expected from the oxide inhomogeneous layers contact with the support. In any case, the anatase/brookite sample can be satisfactorily fitted only using 3 distinct RC elements. From the comparison among the order of magnitude of the three equivalent resistors R$_1$, R$_2$ and R$_3$, we can observe that the resistance describing the anatase/brookite interphase is from 3 to 6 orders of magnitude lower (from MΩ to kΩ or Ω) than those describing the contact between the oxides and the solution or the FTO support. This result can be explained with the very close contact, at the sub–nanometer scale, of the two phases, in agreement with the theoretical and HR–TEM outcomes. It is also worth noting that this interphase can be fitted with a pure capacitor instead of a constant phase element, demonstrating that the separation of charges leads to an almost ideal double layer capacitor with a specific capacitance of 19.6 µF·cm^{-2} (Table 1). This double layer originates from the volume–weighted average of all the nanocapacitors that are associated to individual heterojunctions, which provide a high significance to the EIS estimate. DFT simulations predict a net charge transfer of 5.4 µC·cm^{-2} (Figure S10 SI and Figure 1c) across the interface, in close quantitative agreement with the EIS

outcome (4.2 μC·cm^{-2}, figure 1d). The conformity of views between such estimates is noteworthy, even though it might be partly traced back to some kind of error cancellation, including intrinsic limits of DFT, non–ideality of surfaces and finite–T kinetic effects. The agreement between experiment and theory confirms that a significant amount of nanoheterojunctions involves the most stable $\{101\}_{Anatase}$ and $\{210\}_{Brookite}$ crystallite facets, as shown also by the HR-TEM images in Figure 1a and Figure S1 SI (see above). This is expected, as nanoparticles have been grown under thermodynamic control (Section 1 SI).

In conclusion, an equilibrium double layer is formed (Figure 2a, inset) only when both anatase and brookite are present in the nanostructured powder, in accord with DFT simulations, which predict the brookite (anatase) side as negative (positive) (see above). A standard band-gap alignment where the two phases are calculated separately could not reproduce this representation (Sections S3.2 and S3.5 SI), as there the Valence Band (VB) of brookite is higher in energy by a fraction of eV compared to anatase. However, EIS measurements[27] show that the brookite VB has a lower energy (i.e. a more positive reduction potential), even if for a small amount, in agreement with other experimental estimates (see Fig.6 of Ref.[27]). This means that the anatase VB is bended at lower energies, the brookite one at higher energies, i.e., the brookite-like region can allocate extra electrons at the expenses of the anatase-like one. This VB offset can be directly compared with the T = 0 K ground electronic state calculations results reported above, where a partial electron transfer is observed from anatase–like phase to the brookite–like one, with the consequent formation of a double charge layer. In conclusion, experimental and computational evidences agree that some ground state charge density flows into the brookite lattice, that is, this phase acts as a thermodynamic reducing agent in the anatase:brookite electrochemical pair.

This picture is further corroborated by inspecting at the DFT plane–averaged electrostatic potential along the non–crystallographic direction, which was computed by averaging the quantum

expectation values of the potential from the electronic wavefunction (Section S3.7, Figure 1c). Two quasi–plateaus, each for each polymorph, are neatly visible, the brookite-like one being the most negative. As the averaged potential reflects the distribution of the total charge density, a slight excess of negative charges in the brookite-like region is confirmed. We stress that this is the T = 0 K ground state electronic picture and it does not allows to infer the direction of the charge transfer upon photoexcitation.

Photocurrent measurements

Now we want to see if for our composites, which we now know to be characterized by the presence of a polarized interphase, the generated e^-–h^+ pair recombines significantly slower and by what extent. More specifically, we want to prove that it is the concomitant presence of the two polymorphs, and consequently of their interphase, to be responsible for the e^-–h^+ recombination changes. Photocurrent experiments[47] were performed under UV light (see Methods, Figure 3a and S13 SI). Pristine anatase and the anatase/brookite mixed samples behaved differently, as the corresponding normalized j/j_0 decays required two different least–squares models to provide a satisfactory fitting. This likely indicates the presence of neatly distinguishable decay mechanisms. Usually, the calculation of the transient time constant τ, an estimate of the recombination time, is based on the linearization of the first order exponential decay which describes the first 15/25 seconds of irradiation by the empirical law (1). [47,48]:

$$J(t) = J(0) + A_1 e^{-\frac{t}{\tau_1}} \tag{1}$$

In (1), A_1 is a pre–exponential factor and τ_1 the time constant. The anatase/brookite mixed samples conform with this model (Figure 3b and S14b SI), which correspond to one decay mechanism that

takes place on a second–long timescale (Table 2). A more complex function is needed to model the pristine anatase data (Figure 3a and S14 SI). We found that the bi–exponential decay curve (2) properly fits the pristine anatase data (Figures 3a and Figure S14b SI).

$$J(t) = J(0) + A_1 e^{-\frac{t}{\tau_1}} + A_2 e^{-\frac{t}{\tau_2}} \qquad (2)$$

As shown in Table 2, the first time interval 0–3 seconds is mainly described by an exponential decay characterized by a fast ($\tau_1 \sim 0.4$s) and a slow ($\tau_2 \sim 4$ s) recombination processes, taking place on an one of magnitude larger timescale. Interestingly, these estimates are comparable with those found in multilayer Cr–doped titania[47] and much larger than those attributable to fast $e^- – h^+$ recombination alone. Hence, in pure nano-anatase, two significant slowdown mechanisms are already active, likely due to an extended interconnected network of 3D interphases.

Overall, Eq. (1) implies substantially longer $e^- – h^+$ recombination times in composite MPP TiO_2 nano-powders (Figure 3b). We must conclude that the overall recombination mechanism is different in the biphasic samples, where either the fastest and most efficient recombination route is switched off, or else the slower path dominates. In either case, the effect is to enhance the current density j/j_0 by ~ 40 percent points with respect to pure anatase at $t > 10$ s (Figure 3a,b).
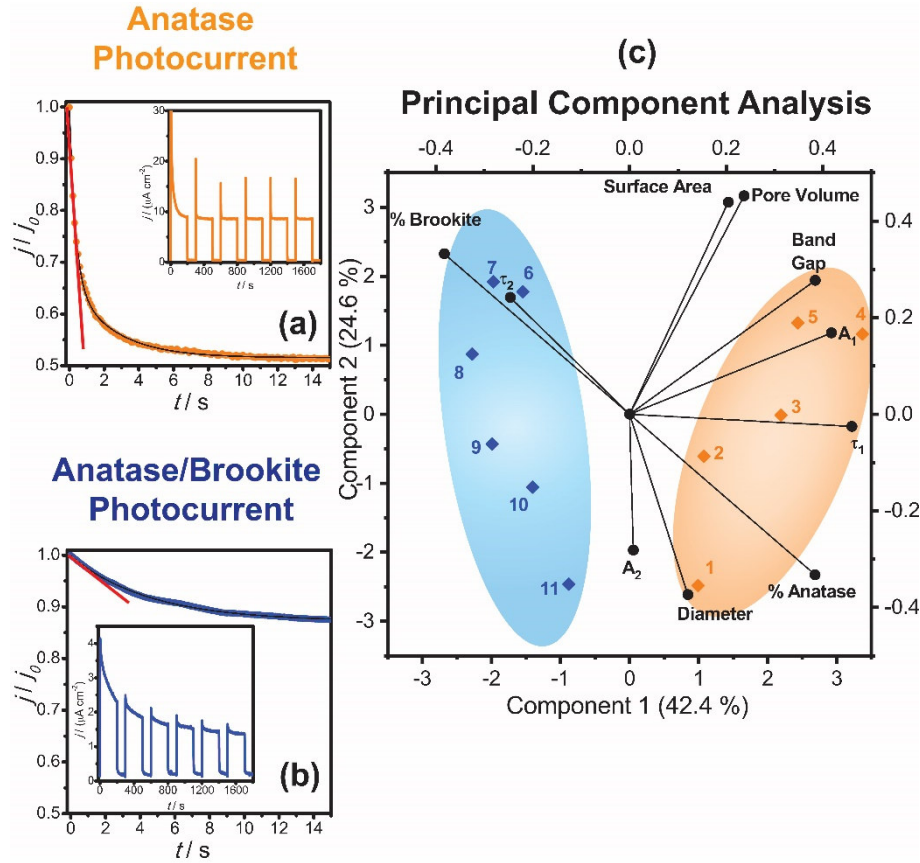
Figure 3. Slow-down of the $e^- – h^+$ recombination time is correlated to the brookite phase presence. (a) Photocurrent measurements on commercial Alfa Aesar 130 anatase (see Table 2). Orange points: normalized j/j_0 current density decay for the first 15 s (4th step of irradiation). Measured data are shown in the inset. Black line: double exponential fit (parameters in Table 3 SI). Red line: first–order Taylor approximation of the exponential function close to t=0 s. (b) Same as (a), for the 96:4 anatase:brookite composite TiO_2 sample (blue points). A single exponential fit (black line) with lower $t{\to}0$ slope (red line) accounts for these data. (c) Principal Component Analysis (PCA)–derived scores (black points) and loadings (black lines) for microstructural parameters of mono– (orange area) and bi–phasic (blue area) TiO_2 powders, showing their correlation with photocurrent estimates (original variables in Table 2). A_1 and A_2 are fitted pre–exponential factors; τ_1 and τ_2 the corresponding recombination times ($\tau_1{\to}0$ for biphasic samples, see Sections S5 and S6 SI). A strong positive correlation is apparent between the τ_2 kinetic constant and the brookite content.

As a further confirmation of the synergistic role played by the anatase/brookite mixing,

photocurrent measurements were also performed on both mono- and bi-phasic TiO_2-based

13

photocatalysts that differed by the *w/w* anatase/brookite ratio, the pore volume, and by the nominal

concentration of the N dopant.

Table 2. Experimental data employed for the Principal Component Analysis study.

Sample	N/Ti[a]	D[b] / nm	% A[c]	% B[c]	SA[d]/ (m² g⁻¹)	V[e] / (mL g⁻¹)	BG[f] / eV	τ_1 / s	τ_2 / s	A₁ x10⁻⁶	A₂ x10⁻⁶
Alfa Aesar 9.5	0	86	100	0	9	0.048	3.2	0.37	3.04	0.40	0.42
Alfa Aesar 42	0	38	100	0	42	0.369	3.15	0.37	4.06	1.73	1.02
Alfa Aesar 130	0	15	100	0	130	0.374	3.19	0.38	2.07	5.60	2.41
Alfa Aesar 284	0	9	100	0	284	0.442	3.35	0.39	2.05	8.43	4.40
Hombikat	0	10	100	0	354	0.352	3.34	0.43	3.08	3.12	1.54
T400	0	7	70	30	170	0.310	3.21	0.0001*	3.08	0.0005*	0.92
TN_0.05	0.05	9	70	30	130	0.480	3.03	0.0003*	4.80	0.0002*	0.62
TN_0.1	0.1	9	77	23	162	0.100	3.38	0.0002*	5.09	0.0004*	1.10
TN_0.2	0.2	10	83	17	98	0.020	3.30	0.0001*	4.03	0.0002*	2.20
TN_0.4	0.4	10	96	4	90	0.010	3.25	0.0002*	4.07	0.0003*	0.21
TN_0,5	0.5	11	93	7	87	0.040	3.25	0.0003*	1.04	0.0007*	16.00

[a] Nominal N/Ti molar ratio
[b] Volume–averaged crystallite dimensions, as obtained from the Scherrer equation applied to the most intense (011) reflection of anatase.
[c] Amount of anatase (A) and brookite (B) content, as estimated from fitting against the relative intensities provided by powder X-ray diffraction patterns (Figure 15c SI).
[d] Specific surface Area (SA) and pore volume (V), as evaluated from BET–BJH analyses (Figure 15a SI).
[f] Apparent band gap (BG), as derived from UV–vis diffuse reflectance spectra (DRS) (Figure 15b SI).
* These values (three orders of magnitude lower than the measured values of the anatase pristine samples) are randomly assigned to avoid biases due to entries exacting equaling 0 in the PCA elaboration.

A Principal Component Analysis (PCA) of the main physical–chemical variables listed in Table 2

(see also Figure 3c) shows that the decay time constant τ_2 correlates with the weight percent of

brookite. In other words, *the phase composition, and not the amount of extrinsic point defects*,

determines the $e^-–h^+$ recombination mechanism. The correlation is not linear, though: the most

brookite–rich powder (score nº 6) has a higher decay rate ($\tau = 3.1$ s) than the EIS–analyzed 77:23

w/w specimen (score nº 7) where $\tau = 5.1$ s. Brookite–poor samples 8–10 all show lower time

constants (Table 2). Likely, they do not bear solid–solid interfaces large enough to produce a net

phase unbalance of the charge carriers. Indeed, nanoparticle size might also influence the nature of

the anatase:brookite double layer, and thus the decay rate. It has been shown that the band level alignment of anatase:rutile nanojunctions depends on quantum confinement effects:[49] the electron transfer at equilibrium might even switch from anatase $\rightarrow$ rutile to rutile $\rightarrow$ anatase upon increasing the dimensions of the nanoparticles in close contact. Whether and to what extent this is also true for anatase:brookite interphases remains to be investigated and might disclose intriguing opportunities to design complex circuit elements at the nanoscale.

Conclusions

This contribution provides a first–principles atomistic description of biphasic TiO_2-based photocatalysts, revealing the formation of a 3D array of anatase-brookite nanodiode-like heterojunctions and correlating it to the enhanced visible–light photocatalytic behavior. In the first part of the paper, we focused on the ground state properties of the interphase nanocapacitor, finding a very good agreement among the hybrid supercell DFT modeling and the electrochemical impedance results. In the second part, we correlated photocurrent outcomes under UV illumination with several structural and compositional parameters, finding a significant, non–trivial correlation among the brookite content and the recombination time. Our interpretative model, based on the atomistic details explaining the electronic interphase balancing, allows the generalization of 2D-heterojunctions to the more ubiquitous 3D case of coexistent crystalline nanoparticles of multi–phase polymorph (MPP) photocatalysts. In particular, TiO_2–MPP devices have several advantages in the context of green chemistry applications: they are easily synthesizable from cheap reactants and environmentally safe. Moreover, crucial parameters like the polymorph ratio and the distribution of the dopant across the nanoparticle can be finely tuned by adjusting a few chemical

and physical degrees of freedom[41,50–52]. Further research is needed to clarify the mechanism of e^-–h^+ recombination delay in the excited states, but our preliminary ground–state results are encouraging and could disclose a new path toward visible–light devices based on this architecture. To this end, we stress the importance of investigating the physics of titania devices at atomistic scale. The recognition of the central role played by MPP nanoheterojunctions could open new exciting scenarios for the tailored synthesis of TiO_2-based semiconductor photocatalysts with superior performances, paving the way toward an entirely novel class of cheap, easily synthesizable and environmental friendly composite materials. We expect that devices based on the MPP heterojunction constructs may lead to important advances in Green Chemistry against contemporary societal challenges

Experimental

Materials

Commercial single–phase TiO_2 powders have been purchased by Alfa Aesar (Anatase 9.5, 42, 130 and 284), Sigma–Aldrich (Brookite) and Sachtleben (Hombikat UV 100) and used without further treatments. Home–made powders, both undoped and N–doped, have been prepared by varying anatase/brookite quantity, following a previously optimized sol–gel synthesis.[52] Nominal N/Ti ratios of 0.05, 0.1, 0.2, 0.4 and 0.5 have been included.

HR–TEM

HR-TEM images were obtained by means of a JEOL 3010–UHR Instrument equipped with a LaB6 filament (acceleration potential 300 kV). All digital micrographs were acquired by an Ultrascan 1000 camera, and the images were processed by Gatan Digital Micrograph program version 3.11.1. Samples were dry dispersed onto Cu grids coated with "lacey" carbon film before the analysis.

DFT calculations.

Simulations have been performed with VASP through a plane wave approach. Projector–augmented pseudopotentials, including spin–polarization, have been used in conjunction with the Perdew–Burke–Ernzerhof GGA parametrization for the exchange–correlation functional. A Hubbard DFT+U splitting has been considered and set to 3.0 eV for the Ti 3d states. The interface model has been built by exposing anatase (101) and brookite (210) surfaces of previously optimized pure phases, and then by putting them in close contact along the non–crystallographic direction as described in Section S3.3 SI. The final model consisted of a 3 nm thick anatase/brookite biphasic slab with 384 atoms, plus a 1.2 nm wide vacuum layer to separate translation–related images of the slab along the non–crystallographic direction. All atoms have been relaxed at constant volume of the simulation box, without imposing any symmetry constraint, with the only exception of the terminal layers in contact with vacuum, which have been kept fixed at their optimized bulk geometries.

Electrochemical Impedance Spectroscopy.

An electrochemical cell with Luggin capillary for ohmic drop abatement, a saturated calomel electrode for reference and electrode setup consisting in two Pt wire counter electrodes perpendicular to working and reference, has been used. The working electrode has been a fluorine–doped tin oxide (FTO) glass covered with a deposition of the desired sample. N_2–deaerated $NaClO_4$ 0.1 M has been employed as supporting electrolyte. Analyses are carried out by using a potentiostat/galvanostat PGStat30 (Autolab, The Netherlands) equipped with a FRA module and Nova 2.0 software.

Photocurrent and photocatalysis.

Photocurrent measurements performed with the same setup as EIS were registered at fixed potential of +1 V (step potential 0.1 s) under 500 W UV light irradiation (Jelosil HG 500, iron halides). The first 600 s represent the dark current, then 200 s of irradiation are alternated with 100 s at dark for 6 times. Photocatalysis experiments were performed using a 300W solar lamp emitting in the 380–600 nm range of wavelengths, with nominal intensity $I = 1.2 \times 10^{-5}$ Einstein dm^{-3} s^{-1}. Reagent–grade methylene blue, NO$_x$ and toluene were the substrates examined.[48,53]

Spectroscopic, BET and diffractometric characterization.

UV–vis spectra were recorded with a UV–vis scanning spectrophotometer (Perkin-Elmer, Lambda 35) equipped with a diffuse reflectance accessory. All spectra were acquired by working in reflectance mode and Kubelka–Munk elaboration is applied for the band gap evaluation. The BET surface area was determined by multipoint BET method using the adsorption data in the relative pressure (p/p$_0$) range of 0.05–0.3. Desorption isotherms were used to determine the pore size distribution using the Barret–Joyner–Halander (BJH) method with cylindrical pore size. XRD diffractograms are obtained with Philips PW 3710 Bragg−Brentano goniometer equipped with a scintillation counter and 1° divergence slit, 0.2 mm receiving slit, and 0.04° Söller slit systems. We employed graphite-monochromated Cu Kα radiation at 40 kV × 40 mA nominal X-rays power. Volume–averaged crystallite dimensions have been estimated through Scherrer equation on (101) anatase and (211) brookite reflections.

Supplementary Information

Supporting Information is available online or from the author.

Correspondence

Correspondence and requests for materials should be addressed to michele.ceotto@unimi.it.

Conflict of interests

There are no conflicts to declare

Ackowledgements

References

1   D. Bozyigit, W. M. M. Lin, N. Yazdani, O. Yarema and V. Wood, *Nat. Commun.*, 2015, **6**, 6180.

2   N. Serpone, A. Salinaro, A. Emeline and V. Ryabchuk, *J. Photochem. Photobiol. A Chem.*, 2000, **130**, 83–94.

3   A. V. Emeline, A. V. Panasuk, N. Sheremetyeva and N. Serpone, *J. Phys. Chem. B*, 2005, **109**, 2785–2792.

4   A. V. Emeline, V. K. Ryabchuk and N. Serpone, *Catal. Today*, 2007, **122**, 91–100.

5   A. V. Emeline, V. N. Kuznetsov, V. K. Rybchuk and N. Serpone, *Int. J. Photoenergy*, 2008, **2008**, 1–19.

6   J. Schneider, M. Matsuoka, M. Takeuchi, J. Zhang, Y. Horiuchi, M. Anpo and D. W. Bahnemann, *Chem. Rev.*, 2014, **114**, 9919–9986.

7   Y. Ma, X. Wang, Y. Jia, X. Chen, H. Han and C. Li, *Chem. Rev.*, 2014, **114**, 9987–10043.

8   F. Spadavecchia, G. Cappelletti, S. Ardizzone, M. Ceotto, M. S. Azzola, L. Lo Presti, G. Cerrato and L. Falciola, *J. Phys. Chem. C*, 2012, **116**, 23083–23093.

9   M. Ceotto, L. Lo Presti, G. Cappelletti, D. Meroni, F. Spadavecchia, R. Zecca, M. Leoni, P. Scardi, C. L. Bianchi and S. Ardizzone, *J. Phys. Chem. C*, 2012, **116**, 1764–1771.

10   W. Choi, A. Termin and M. R. Hoffmann, *J. Phys. Chem.*, 1994, **98**, 13669–13679.

11   G. Rothenberger, J. Moser, M. Graetzel, N. Serpone and D. K. Sharma, *J. Am. Chem. Soc.*, 1985, **107**, 8054–8059.

12   A. Selloni and S. A., *Nat. Mater.*, 2008, **7**, 613–615.

13   S. Selcuk and A. Selloni, *Nat. Mater.*, 2016, **15**, 1107–1112.

14   H. G. Yang, C. H. Sun, S. Z. Qiao, J. Zou, G. Liu, S. C. Smith, H. M. Cheng and G. Q. Lu, *Nature*, 2008, **453**, 638–641.

15   M. Pelaez, N. T. Nolan, S. C. Pillai, M. K. Seery, P. Falaras, A. G. Kontos, P. S. M. Dunlop, J. W. J. Hamilton, J. A. Byrne, K. O'Shea, M. H. Entezari and D. D. Dionysiou, *Appl. Catal. B Environ.*, 2012, **125**, 331–349.

16   S. Horikoshi and N. Serpone, *Catal. Today*, 2020, **340**, 334–346.

17   A. V. Emeline, V. N. Kuznetsov, V. K. Ryabchuk and N. Serpone, *Environ. Sci. Pollut. Res.*, 2012, **19**, 3666–3675.

18   N. Serpone and A. V. Emeline, *J. Phys. Chem. Lett.*, 2012, **3**, 673–677.

19   G. Di Liberto, S. Tosoni and G. Pacchioni, *J. Phys. Condens. Matter*, 2019, **31**, 434001.

20   C. Huang, S. Wu, A. M. Sanchez, J. J. P. Peters, R. Beanland, J. S. Ross, P. Rivera, W. Yao, D. H. Cobden and X. Xu, *Nat. Mater.*, 2014, **13**, 1096–1101.

21   H. Wang, L. Zhang, Z. Chen, J. Hu, S. Li, Z. Wang, J. Liu and X. Wang, *Chem. Soc. Rev.*, 2014, **43**, 5234.

22   J. P. Colinge and C. A. Colinge, *Physics of Semiconductor Devices*, Kluwer Academic Publishers, NEW YORK, BOSTON, DORDRECHT, LONDON, MOSCOW, 1st edn., 2002.

23   G. Di Liberto, V. Pifferi, L. Lo Presti, M. Ceotto and L. Falciola, *J. Phys. Chem. Lett.*, 2017, **8**, 5372–5377.

24   F. A. Ponce and D. P. Bour, *Nature*, 1997, **386**, 351–359.

25   L. Marona, D. Schiavon, M. Baranowski, R. Kudrawiec, I. Gorczyca, A. Kafar and P. Perlin, *Sci. Rep.*, 2020, **10**, 1235.

26   V. Pifferi, G. Soliveri, G. Panzarasa, S. Ardizzone, G. Cappelletti, D. Meroni and L. Falciola, *RSC Adv.*, 2015, **5**, 71210–71214.

27   A. Di Paola, M. Bellardita and L. Palmisano, *Catalysts*, 2013.

28   N. K. Elumalai, C. Vijila, R. Jose, A. Uddin and S. Ramakrishna, *Mater. Renew. Sustain. Energy*, 2015.

29   A. Di Paola, M. Bellardita, R. Ceccato, L. Palmisano and F. Parrino, *J. Phys. Chem. C*, 2009, **113**, 15166–15174.

30   Y. Liao, W. Que, Q. Jia, Y. He, J. Zhang and P. Zhong, *J. Mater. Chem.*, 2012, **22**, 7937.

31   S. Pitchaimuthu, K. Honda, S. Suzuki, A. Naito, N. Suzuki, K. I. Katsumata, K. Nakata, N. Ishida, N. Kitamura, Y. Idemoto, T. Kondo, M. Yuasa, O. Takai, T. Ueno, N. Saito, A. Fujishima and C. Terashima, *ACS Omega*, 2017, **3**, 898–905.

32   H. Zhao, L. Liu, J. M. Andino and Y. Li, *J. Mater. Chem. A*, 2013, **1**, 8209–8216.

33   J. Liu, W. Qin, S. Zuo, Y. Yu and Z. Hao, *J. Hazard. Mater.*, 2009, **163**, 273–278.

34   G.-S. Shao, X.-J. Zhang and Z.-Y. Yuan, *Appl. Catal. B Environ.*, 2008, **82**, 208–218.

35   Z. Pap, L. Baia, K. Mogyorósi, A. Dombi, A. Oszkó and V. Danciu, *Catal. Commun.*, 2012, **17**, 1–7.

36   D. O. Scanlon, C. W. Dunnill, J. Buckeridge, S. A. Shevlin, A. J. Logsdail, S. M. Woodley, C. R. A. Catlow, M. J. Powell, R. G. Palgrave, I. P. Parkin, G. W. Watson, T. W. Keal, P. Sherwood, A. Walsh and A. A. Sokol, *Nat. Mater.*, 2013, **12**, 798–801.

37   G. Li and K. A. Gray, *Chem. Phys.*, 2007, **339**, 173–187.

38   Y. Gao, J. Zhu, H. An, P. Yan, B. Huang, R. Chen, F. Fan and C. Li, *J. Phys. Chem. Lett.*, 2017, **8**, 1419–1423.

39   Y. Wei, Z. Zhou, W. H. Fang and R. Long, *J. Phys. Chem. Lett.*, 2018, **9**, 5884–5889.

40   K. Ozawa, M. Emori, S. Yamamoto, R. Yukawa, S. Yamamoto, R. Hobara, K. Fujikawa, H. Sakama and I. Matsuda, *J. Phys. Chem. Lett.*, 2014, **5**, 1953–1957.

41   L. Lo Presti, M. Ceotto, F. Spadavecchia, G. Cappelletti, D. Meroni, R. G. Acres and S. Ardizzone, *J. Phys. Chem. C*, 2014, **118**, 4797–4807.

42   G. Liu, H. G. Yang, J. Pan, Y. Q. Yang, G. Q. M. Lu and H.-M. Cheng, *Chem. Rev.*, 2014, **114**, 9559–9612.

43   W. K. Li, X. Q. Gong, G. Lu and A. Selloni, *J. Phys. Chem. C*, , DOI:10.1021/jp802335h.

44   L. Glasser and H. D. B. Jenkins, *J. Am. Chem. Soc.*, , DOI:10.1021/ja992375u.

45   R. F. W. Bader, *Atoms in Molecules: A Quantum Theory, International Series of Monographs on Chemistry 22*, 1990.

46   D. Koch and S. Manzhos, *J. Phys. Chem. Lett.*, 2017, **8**, 1593–1598.

47   R. Dholam, N. Patel, A. Santini and A. Miotello, *Int. J. Hydrogen Energy*, 2010, **35**, 9581–9590.

48   F. Spadavecchia, S. Ardizzone, G. Cappelletti, L. Falciola, M. Ceotto and D. Lotti, *J. Appl. Electrochem.*, 2013, **43**, 217–225.

49   K. C. Ko, S. T. Bromley, J. Y. Lee and F. Illas, *J. Phys. Chem. Lett.*, 2017, **8**, 5593–5598.

50   C. Marchiori, G. Di Liberto, G. Soliveri, L. Loconte, L. Lo Presti, D. Meroni, M. Ceotto, C. Oliva, S. Cappelli, G. Cappelletti, C. Aieta, S. Ardizzone, G. Di Liberto, G. Soliveri, L. Loconte, L. Lo Presti, D. Meroni, M. Ceotto, C. Oliva, S. Cappelli, G. Cappelletti, C. Aieta and S. Ardizzone, *J. Phys. Chem.*, 2014, **118**, 24152−24164.

51   F. Spadavecchia, M. Ceotto, L. Lo Presti, C. Aieta, I. Biraghi, D. Meroni, S. Ardizzone and G. Cappelletti, *Chinese J. Chem.*, 2014, **32**, 1195–1213.

52   L. Rimoldi, C. Ambrosi, G. Di Liberto, L. Lo Presti, M. Ceotto, C. Oliva, D. Meroni, S. Cappelli, G. Cappelletti, G. Soliveri and S. Ardizzone, *J. Phys. Chem. C*, 2015, **119**, 24104–24115.

53   F. Spadavecchia, G. Cappelletti, S. Ardizzone, C. L. Bianchi, S. Cappelli, C. Oliva, P. Scardi, M. Leoni and P. Fermo, *Appl. Catal. B Environ.*, 2010, **96**, 314–322.

Graphical Abstract
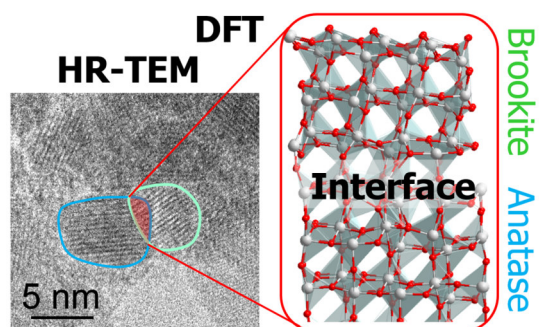
Description: A change of view for anatase/brookite 2D-heterojunctions into 3D patchworks of intimately associated mixed crystallites allows us to model the interphase as a nanocapacitor able to facilitate charge separation and photocatalysis.

Keywords: Computational chemistry, Density functional calculations, Electrochemistry, Interfaces, Nanoparticles